Soft Matter

Stress-structure relation in dense colloidal melt under forward and instantaneous reversal of shear

SCHOLARONE™
Manuscripts

Stress-structure relation in dense colloidal melt under forward and instantaneous reversal of shear

Amit Kumar Bhattacharjee[1, *]

[1]*Fachbereich Physik, Universität Konstanz, 78457 Konstanz, Germany*
(Dated: May 9, 2015)

Dense supercooled colloidal melt in forward shear from a quiescent state shows overshoot in shear stress at 10% strain with an unchanged fluid structure at equal stress before and after overshoot. In addition, we find overshoot in normal stress with a monotonic increase in osmotic pressure at an identical strain. The first and second normal stress become comparable in magnitude and opposite in sign. Functional dependence of the steady state stress and osmotic pressure with Péclet number demonstrate signature of crossover between Newtonian and nearly- Newtonian regime. Moreover, instantaneous shear reversal from steady state exhibit Bauschinger effect, where strong history dependence is observed depending on the time of flow reversal. The distribution of particulate stress and osmotic pressure at the point of flow reversal is shown to be a signature of the subsequent response. We link the history dependence of the stress-strain curves to changes in the fluid structure measured through the angular components of the radial distribution function. A uniform compression in transition from forward to reversed flowing state is found.

I. INTRODUCTION

The mechanical and structural response of dense colloidal dispersion under external forces are intriguing due to the interplay of associated single particle relaxation time scale τ_0 and the structural relaxation time scale τ, many orders of magnitude slower than the previous. A rich behaviour of amorphous solid like and non-Newtonian fluid like behaviour is seen in experiments and simulations when perturbed on a timescale $1/\dot{\gamma}$ with $\tau_0 \ll \dot{\gamma}^{-1} \ll \tau$ [1]. Fluid like behaviour is exemplified by an increase in the shear viscosity referred as shear thinning or thickening, while the solid like behaviour through the finite yield stress and nonzero elastic constants of the media [2]. Non-Newtonian fluids also exhibit nonzero normal stress components, signs of them lead to compression or propulsion of fluid mass leading to fascinating phenomena *e.g.* rotating rod flows [3] and rod climbing effects in attractive colloids [4]. The flowing steady state response is usually characterized as a nonlinear function of $\dot{\gamma}$ by the macroscopic shear stress σ_{xy}. In addition, first and second normal stress together with osmotic pressure as a function of $\dot{\gamma}$ must be sought to characterize the stress tensor. Nonlinear functional form of shear and normal stresses with Péclet number as well as a positive first normal stress and a sign reversed second normal stress for monodisperse colloidal suspensions at lower and moderately high volume fractions had been reported in Stokesian dynamics simulation of concentrated colloidal suspension [5] as well as molecular dynamics (MD) simulation of non-Brownian spheres [6]. Similar results are reported in system with charge-stabilized dispersion [7], however the functional dependence in vicinity of glass transition are not known.

In addition to the study of steady state properties, rigorous theoretical, experimental as well as simulational emphasis has been employed in past couple of decades to study the transient response of various systems in external shear to understand the kinetic pathway through which these systems evolve to steady flowing state. As a constant strain rate is applied to a quiescent state at $t = 0$, shear stress increase from zero to a steady-state value with an intermediate hump at 10% strain amplitude for dense colloids, known in the literature as stress overshoot. These overshoot phenomena is reported in the MD simulations and experiments of gels [8], dense polymeric melts [9], liquid crystalline polymers [10] and charged as well as uncharged dense colloidal melt [11–13]. The last example is reasonably well understood within the mode coupling theory (MCT) framework. An internal connection between superdiffusive particulate motion and jump in the local stress variances has been attributed to the stress overshoot.

Considerable emphasis has also been exercised to understand a connection between shear-deformed microstructure and the macroscopic stresses [14–16]. A universal flow-induced structure at equal stresses have emerged at the elastic and plastic branch of the stress-strain curve. Application of shear deformation at constant rate leads to a modification of the stress overshoot in a system quenched into its glassy state: after startup flow, shear is reversed in the steady state leading to a vanishing of the maximum in the stress-strain curve known as the Bauschinger effect [12, 17]. The effect has been analyzed in terms of anisotropic athermal elastic constants that arise since the initially isotropic amorphous state acquires anisotropy under the initial deformation. A gradual disappearance of the shear stress overshoot as well as ceasing superdiffusion is found by the successive flow reversal from intermediate states to the steady flowing state. The transient and steady state properties of osmotic pressure is difficult to measure in experiments and recently been computed in computer simulations [18]. To

* Present Address: Courant Institute of Mathematical Sciences, New York University, New York, NY 10012; Email address: amitb@courant.nyu.edu

our knowledge, the transient and steady state response in terms of the macroscopic quantities and their relation to the shear-deformed microstructure under various flow history is yet to be sought.

Here we investigate the nonlinear rheology under start up flow from equilibrated state as well as in instantaneous flow reversal from intermediate and steady flowing states, without referring to the athermal variant. The issues that we address here can be categorized into: (a) the transient and steady state response of the stresses and osmotic pressure to steady shear and response to instantaneous reversal of shear, (b) connection between Bauschinger effect and the particulate stresses and (c) the flow-induced structural response of the melt in transient and steady flowing states and their relation with the macroscopic stresses.

The article is organized as follows: Section II gives a concise overview of the simulation method while Sec. III pre-empts the results through an establishment of the connection between the mechanical response to the fluid microstructure. We discuss the central results in Sec IV and Sec. V concludes.

II. SIMULATION METHODS

We simulate a model system of dense supercooled colloidal suspension through nonequilibrium molecular dynamics simulation. An additive binary mixture of size ratio 1.2 is chosen to avoid crystallization as well as artifacts due to large size disparity. The components interact within a cutoff distance $r < r_{c,\alpha\beta}(= 2^{1/6}\sigma_{\alpha\beta})$ through a purely-repulsive soft-sphere WCA potential [19], $V_{\alpha\beta}(r) = 4\epsilon_{\alpha\beta}\left[\left(\frac{\sigma_{\alpha\beta}}{r}\right)^{12} - \left(\frac{\sigma_{\alpha\beta}}{r}\right)^6 + \frac{1}{4}\right]S_{\alpha\beta}(r)$ where σ denotes the particle diameter and α, β the particle species. $S_{\alpha\beta}(r) = (r - r_{c,\alpha\beta})^4/[h^4 + (r - r_{c,\alpha\beta})^4]$ with $h = 10^{-2}\sigma_{\alpha\beta}$ is a smoothing function applied to ensure continuity of force and conservation of total energy in the NVE ensemble. Both species are assigned equal masses for convenience. Units of energy $\epsilon_{\alpha\beta} = 1$ and units of length are so chosen that $\sigma_{AA} = 1$ and the unit of time is $\tau = \sqrt{m_A\sigma_{AA}^2/\epsilon_{AA}}$ where m_A is the mass of A-species of particles. The simulation consisted of $N = 2N_A = 1300$ particles in a three-dimensional box with linear dimension $L = 10\sigma_{AA}$, corresponding to a number density $\rho = 1.3/\sigma_{AA}^3$ [12].

Colloidal property is incorporated in the mixture by coupling to a dissipative particle dynamics (DPD) thermostat where the dissipative force, proportional to the relative velocity of two species of particles, ensures Galilean invariance thereby local conservation of momentum. The random force satisfying fluctuation dissipation relation ensures Boltzmann distribution in equilibrium. These two competing force sets uniquely the temperature of the system. The cut off radius for the thermostat is chosen to be $1.7r_{c,\alpha\alpha}$ and the controlling parameter for frictional forces is set to $\zeta = 10$.

The Langevin equation of motion are integrated with a generalized velocity Verlet algorithm with a time increment of $\delta t = 5 \times 10^{-4}$. Our estimation of the glass transition point according to MCT description is $T_c \approx 0.347$ and we focus our work on the equilibrated fluid at $T = 0.4$. Initial equilibration is proceeded by step increments of $\delta t = 10^{-3}$, assigning new velocities on every 50 integration time steps. The simulation runs were long enough to observe the decay of the incoherent intermediate scattering function to zero for a wave number corresponding to a typical interparticle separation. A set of 1000 independently equilibrated configurations served as initial configurations for the forward shear runs, while 1000 pre-sheared configurations for three separate strains are chosen for shear reversal runs employing the DPD thermostat.

Shear is applied from strain-free configurations in the x-direction with a gradient in the y-direction (thus, vorticity along z-direction) at a fixed strain rate $\dot\gamma = 5 \times 10^{-3}$ initially for 3×10^7 steps resulting to steady state with strain $\gamma = 75$. Shear is reversed and proceeded from three pre-sheared states, denoted with strain $-\gamma_w^{el} = 3.5 \times 10^{-2}$, $-\gamma_w^{max} = 8.6 \times 10^{-2}$ and $-\gamma_w^s = 75$ for 3×10^7 simulation steps, resulting to steady states with accumulated strain $-74.965, -74.914$ and 0. For all these cases, planar Couette flow is imposed by periodic Lees-Edwards boundaries and an establishment of linear velocity profile is achieved within a few iterations.

III. CONNECTION BETWEEN STRESSES AND MICROSTRUCTURE

The amount of stress developed by the application of steady shear to a quiescent unsheared state or pre-sheared states are measured through the nonzero components of the stress tensor $\sigma_{\mu\nu}$. Kirkwood formula defines a combination of kinematic and virial contribution to the stress tensor [14],

$$\sigma_{\mu\nu} = \langle\hat\sigma_{\mu\nu}\rangle = -\frac{1}{V}\left\langle\sum_{i=1}^{N}\left[m_i v_{i,\mu}v_{i,\nu} + \sum_{j\neq i}r_{ij,\mu}F_{ij,\nu}\right]\right\rangle \tag{1}$$

where the angular brackets are indicative of canonical averaging, i, j denote the particle index and μ, ν are the Cartesian directions. In a specified coordinate system having shear along x direction with a gradient along y direction, the dominant contribution to the shear stress is the off-diagonal xy-element and the normal stresses are the combination of the diagonal xx, yy and zz-element of the stress tensor. The first and second normal stresses are the differences in the diagonal components as [2],

$$\mathcal{N}_1 = \langle\sigma_{xx} - \sigma_{yy}\rangle; \ \mathcal{N}_2 = \langle\sigma_{yy} - \sigma_{zz}\rangle. \tag{2}$$

and the third normal stress $\mathcal{N}_3$ is the sum of the two. The osmotic pressure is the sum of the diagonal elements

of the stress tensor,

$$\mathcal{P} = -\frac{1}{3} \langle \sigma_{xx} + \sigma_{yy} + \sigma_{zz} \rangle. \tag{3}$$

The virial part of the stress tensor in Eq.(1) can be expressed in terms of the pair distribution function $g^{\alpha\beta}(\mathbf{r}) = V/N_\alpha N_\beta \times \langle \sum_{i=1}^{N_\alpha} \sum_{j(\neq i)}^{N_\beta} \delta(\mathbf{r} - |\mathbf{r}_i^\alpha - \mathbf{r}_j^\beta|) \rangle$ by rewriting the equation and substituting expressions for pairwise force in the following manner [14],

$$\sigma = -\frac{1}{2V} \langle \sum_{i=1}^{N_\alpha} \sum_{j(\neq i)}^{N_\beta} \mathbf{r}_{ij} \mathbf{F}_{ij} \rangle, \tag{4}$$

$$= -\frac{1}{2V} \langle \int d\mathbf{r} \sum_{\alpha,\beta} \sum_{i=1}^{N_\alpha} \sum_{j(\neq i)}^{N_\beta} \delta(\mathbf{r} - |\mathbf{r}_i^\alpha - \mathbf{r}_j^\beta|) \mathbf{r} \mathbf{F}_{ij} \rangle,$$

$$= \frac{1}{2V} \langle \int d\mathbf{r} \sum_{\alpha,\beta} \sum_{i=1}^{N_\alpha} \sum_{j(\neq i)}^{N_\beta} \delta(\mathbf{r} - |\mathbf{r}_i^\alpha - \mathbf{r}_j^\beta|) \frac{\mathbf{rr}}{r} \frac{\partial V_{\alpha\beta}}{\partial r} \rangle,$$

$$= \frac{1}{2V^2} \int d\mathbf{r} \sum_{\alpha,\beta} N_\alpha N_\beta \frac{\mathbf{rr}}{r} \frac{\partial V_{\alpha\beta}}{\partial r} g^{\alpha\beta}(\mathbf{r})$$

$$= \frac{\rho^2}{2} \int d\mathbf{r} \sum_{\alpha,\beta} \frac{N_\alpha N_\beta}{N^2} \frac{\mathbf{rr}}{r} \frac{\partial V_{\alpha\beta}}{\partial r} g^{\alpha\beta}(\mathbf{r})$$

where $\rho = N/V$ is the average density and N_α, N_β correspond to the number of particles of the respective species index.

Shear induced pair distribution function for either forward or backward directed sheared states does not exhibit any significant structural change compared to the quiescent state. A more relevant quantity sensitive to shear is constructed [14–16], where the three dimensional pair correlation function is expanded into the basis of spherical harmonics as, $g^{\alpha\beta}(\mathbf{r}) = \sum_l \sum_m g_{lm}^{\alpha\beta}(r) Y_{lm}(\theta, \phi)$. Here $Y_{lm}(\theta, \phi) = (-1)^m \sqrt{\frac{2l+1}{4\pi} \frac{(l-m)!}{(l+m)!}} P_{lm}(cos\theta) e^{im\phi}$ are the spherical harmonics of degree l and order m, θ and ϕ are the polar and azimuthal angle and $P_{lm}(cos\theta)$ are the associated Legendre polynomial [20]. From symmetry considerations, only even numbers in l is existent and the most relevant terms in the expansion are associated to $l = 2, m = 0, \pm 2$. Here we look for in-plain structural changes to shear and the relevant expansion coefficients associated to $g(r)$ are,

$$Re[g_{22}^{\alpha\beta}(r)] = \sqrt{\frac{15}{16\pi}} \frac{V}{N_\alpha N_\beta} \langle \sum_{i=1}^{N_\alpha} \sum_{j(\neq i)}^{N_\beta} \delta(r - |\mathbf{r}_i^\alpha - \mathbf{r}_j^\beta|)$$

$$\times \frac{(x_i^\alpha - x_j^\beta)^2 - (y_i^\alpha - y_j^\beta)^2}{r^4} \rangle \tag{5}$$

$$Im[g_{22}^{\alpha\beta}(r)] = \sqrt{\frac{15}{8\pi}} \frac{V}{N_\alpha N_\beta} \langle \sum_{i=1}^{N_\alpha} \sum_{j(\neq i)}^{N_\beta} \delta(r - |\mathbf{r}_i^\alpha - \mathbf{r}_j^\beta|)$$

$$\times \frac{(x_i^\alpha - x_j^\beta)(y_i^\alpha - y_j^\beta)}{r^4} \rangle \tag{6}$$

where Re and Im represent the real and imaginary part. Both these components are nonexistent in the quiescent state while they accumulate values in the sheared states. Integrating the algebraic combination of these functions together with the interparticle force yields the first normal stress [21] as well as the shear stress [16, 21],

$$\mathcal{N}_1 = \rho^2 \sqrt{\frac{2\pi}{15}} \sum_{\alpha\beta} \frac{N_\alpha N_\beta}{N^2} \int_0^\infty dr r^3 \frac{\partial V_{\alpha\beta}(r)}{\partial r}$$

$$\times Re[g_{22}^{\alpha\beta}(r)], \tag{7}$$

$$\sigma_{xy} = -\rho^2 \sqrt{\frac{2\pi}{15}} \sum_{\alpha\beta} \frac{N_\alpha N_\beta}{N^2} \int_0^\infty dr r^3 \frac{\partial V_{\alpha\beta}(r)}{\partial r}$$

$$\times Im[g_{22}^{\alpha\beta}(r)]. \tag{8}$$

IV. RESULTS

We summarize the main findings in the dynamics and microstructure of the colloidal melt under shear startup and instantaneous shear reversal.

A. Dynamics

1. Flow curve

Fig.(1) shows the flow curve, that is the steady state scaling of the shear stress, first and second normal stresses and the osmotic pressure with the corresponding Péclet number (Pe) in forward shear at fixed temperature $T = 0.4$. The structural relaxation timescale of the supercooled melt at this temperature is computed to be $\tau_\alpha = 1.8 \times 10^3$, which is slower by a factor of 10^4 than a single particle relaxation time. Panel (a) depicts an increase in σ_{xy} with increasing Pe which is a typical mechanical response of the melt, with a crossover from Newtonian to sub-Newtonian scaling regime for $Pe > 0.1$, that corresponds to strain rates higher than $\dot{\gamma} = 10^{-4}$. It is to notice that above T_c, there exists no finite yield stress and the low Pe response is always Newtonian, as been expected in a dense liquid mixture. However, we find that both first and second normal stresses remain in the sub-Newtonian regime for $Pe > 1$. As noted in fig.(1) caption on the power law scaling of stresses with Pe, scaling exponents of normal stresses are higher than the shear stress exponent. This results to a slower transition from Newtonian to sub-Newtonian regime for normal stresses than the shear stress, thus explaining the depicted behaviour of the stresses at moderate values of Pe. We expect the low shear rate response of both stresses to be Newtonian. In Panel (b), we depict the osmotic pressure as a function of Pe. The pressure decreases with decreasing Pe and saturates for $Pe < 0.1$. The low Pe response of pressure is thus independent of Pe and reaches to the quiescent state value. On the other hand for moderately high values of Pe, pressure and shear stress grows in a
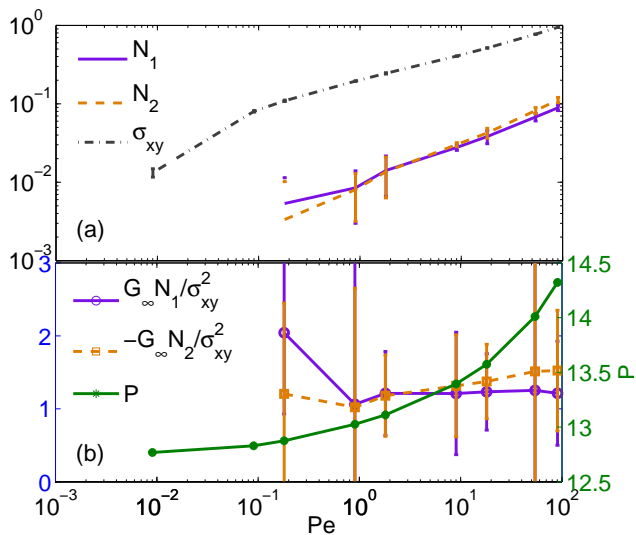
FIG. 1. (Color online) Scaling of the steady state normal stresses $\mathcal{N}_{1,2}$, shear stress σ_{xy} [panel (a)] and osmotic pressure P [panel (b)] with Péclet number Pe in forward shear. Panel(b) also shows the scaling of $G_\infty \mathcal{N}_{1,2}/\sigma_{xy}^2$ with Pe. The effective scaling laws are found to be $\sigma_{xy} \sim (Pe)^{0.36}$, $N_1 \sim (Pe)^{0.51}$, $N_2 \sim (Pe)^{0.58}$ and $P \sim (Pe)^{0.37}$ respectively. A total of 400 independent simulation runs are averaged for strain rates below 5×10^{-4} for statistics while 100 averages were sufficient for higher strain rates to obtain the graphics.
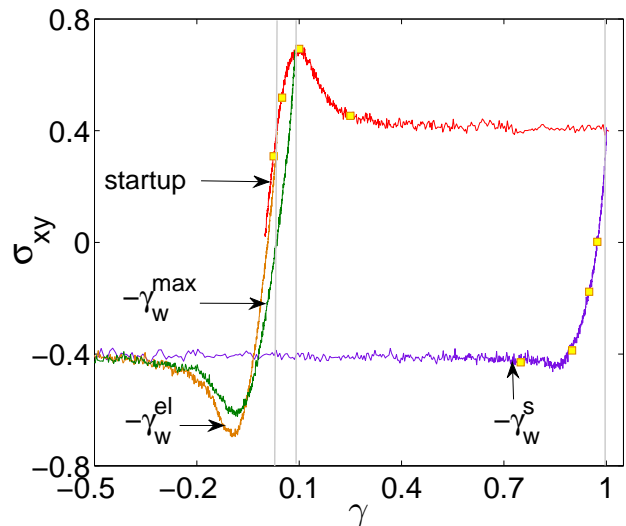

FIG. 2. (Color online) Linear plot of stress-strain relation $\sigma_{xy}(\gamma)$ at fixed temperature and strain rate for various flow histories: (i) starting from equilibrium (startup, red), (ii) after flow reversal in the steady state (-γ_w^s, magenta), (iii) from the elastic regime (-γ_w^{el}, brown) and (iv) from point of the stress overshoot (-γ_w^{max}, green). Abscissa of the -γ_w^s curve is shifted from $\gamma = 75$ to $\gamma = 1$ for comparison. The vertical bars in gray denote the successive points of shear-reversal from elastic, overshoot and steady state regime of the startup curve. Square (yellow) dots, corresponding to the accumulated strain indicated in fig.(5), are printed on startup and steady state reversed curve. A total of 200 independent configurations are averaged to obtain the graphics.

similar fashion, reflected also in the power law scaling exponents. Similar response in pressure is also reported in simulations of hard-sphere glass [22].

Another quantity of interest is the dimensionless number $G_\infty \mathcal{N}_{1,2}/\sigma_{xy}^2$ with G_∞ denoting the low frequency plateau modulus. For moderately high shear rates, shear-thinning generalized Maxwell model predicts, $\sigma_{xy} = G_\infty \gamma$ and $\mathcal{N}_{1,2} = 2G_\infty \gamma^2$ where γ is the strain. Therefore $G_\infty \mathcal{N}_{1,2}/\sigma_{xy}^2 = 2$ [23]. Pe-dependence of this quantity is displayed in panel (b). For an increasing Pe, the ratio progresses towards a value ~ 2. This result thus restricts the applicability of the model at the considered range of Pe numbers.

2. Shear stress response

Next we draw our attention in studying the transient response of the melt under forward and instantaneous reversal of the direction of applied shear. Fig.(2) depicts the shear stress as a function of strain $\gamma = \dot{\gamma}t$ for fixed strain rate $\dot{\gamma}$ and time t. Stress is measured after application of the strain rate to equilibrated configurations and after shear reversal from three different flowing states. In forward shear at a strain around $\gamma \approx 10\%$, a profound stress overshoot from the steady state stress value is observed, found earlier in studies of binary colloidal melt with screened long ranged interaction [11]. State-of-the-art explanation of this behaviour follows as

the enhancement of energies transferred by the shearing forces to the particles caged within their immediate neighbours with a characteristic length: the Lindemann length. At any strain lower than the denoted strain, the mechanical response of the mixture is that of an elastic solid with finite G_∞ ($\sigma_{xy} \sim G_\infty \gamma$). Considering the time scales involved, the initial part of the $\sigma_{xy}(\gamma)$ curve for low strain rates is dominated by the long-time plateau modulus G_∞ rather than the instantaneous modulus G_0. At large strains however, the response is that of a viscous fluid where σ_{xy} is not a function of γ, but of $\dot{\gamma}$. Strains of order unity appear sufficient to drive the system into this state of steady flow. This is consistent with the expectation that the flow-induced decay of correlations occurs on a time scale set by $\dot{\gamma}^{-1}$. The argument leading to this state follows as the release of elastic energy from the breaking of local cages, that leads also to superdiffusive particle motion in between the ballistic and diffusive motion, reported in the study of mean squared particle displacement [11, 12]. Reversing the direction of the applied shear at various strains along the stress-strain curve results in an accumulated strain that first decreases to zero. After that, $|\gamma|$ grows linearly as a function of time. In steady flowing state, $|\gamma| \to \infty$ asymptote is $-\sigma_s(\dot{\gamma})$ where σ_s is the steady state stress at forward shear. Hence in

fig.(2), different $\sigma_{xy}(\gamma)$ curves in shear reversal coincide at large strains.

Comparing the steady state reversal curve with the initial startup curve, the most striking difference is the absence of a stress overshoot. This agrees with the findings of ref.[17], where the same phenomenology was reported for a system quenched initially into the glassy state. As a consequence, the steady-state value of the stress is reached earlier than the startup case at a value, slightly higher than the accumulated strain of $|\gamma| \approx 0.1$. This is somewhat surprising, since one might expect the pre-sheared state to bear structural anisotropies that accommodate flow in the $+x$ direction and hence oppose that in the $-x$ direction more than the isotropic equilibrium structure. This appears not the case in our simulation, that we elaborate more while discussing on the local microstructure. This is corroborated also by looking at the instantaneous effective elastic modulus, $G_{\text{eff}} = d\sigma/d\gamma|_{|\gamma-\gamma_0|=0.025}$ (γ_0 being the strain when stress first decreases to zero): a lower value is found following flow reversal than the one characterizing the initial startup from the equilibrium configuration [12].

Flow reversal inside the elastic transient results in a stress-strain curve that exhibits a negative stress overshoot, displayed in fig.(2) labeled with $-\gamma_w^{el}$. The magnitude of the overshoot is identical to the initial startup flow. This exemplifies that during the elastic part, strain-induced rearrangements are essentially reversible, unlike in the plastic regime of viscous flow. The figure also depicts the case of flow reversal, once the initial stress-strain curve has reached its maximum (curve labeled with $-\gamma_w^{max}$). This intermediate case still exhibits a pronounced overshoot, albeit lower than the $-\gamma_w^{el}$ case. Thus, up to the stress overshoot, the response of the system to the initial flow is mainly reversible. This is consistent with the notion that the overshoot marks the nontrivial breaking of nearest neighbour cages due to the imposed flow. We want to remind the reader that an overshoot in $\sigma_{xy}(\gamma)$ implies a dynamic shear modulus or microscopic stress autocorrelation function that exhibits overrelaxation: stresses do not simply decorrelate but, during breaking of cages, are released in such a way that they briefly become anti-correlated during the process [11].

3. Transient dynamics of normal stresses

To complete the discussion on stresses, we study the transient and steady state response of normal stresses, defined in Eq.(2), as a function of strain. Panel (a) of fig.(3) depicts $\mathcal{N}_1$ and $\mathcal{N}_2$ as a function of strain γ for the startup shear from quiescent configuration, while panel (b) display results in shear reversal from the steady state, after shear stress becomes negative. The magnitude of the normal stress is noted approximately one order smaller than that of shear stress, which can be anticipated to the quadratic scaling of normal
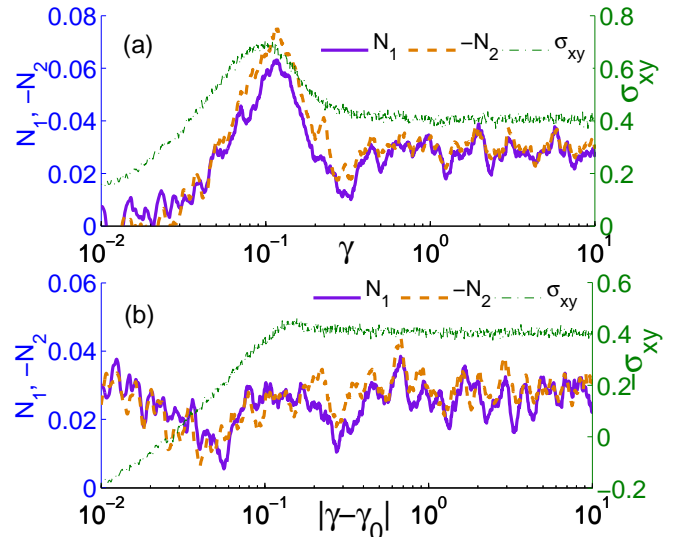

FIG. 3. (Color online) Semilog plot of the normal stress-strain relation $\mathcal{N}_{1,2}(\gamma)$ at fixed temperature and strain rate for two different flow histories: panel (a): shear start up from a quiescent state and panel (b): shear reversal from a steady flowing state (denoted with $-\gamma_w^s$ in fig.2). For comparison, shear stresses in both situations are depicted. A total of 1000 independent simulation runs are averaged to obtain the graphics.

stress with Pe. For startup case, $\mathcal{N}_1$ builds up to attain steady state value after exhibiting an overshoot around 10% of strain, very similar to the shear stress-strain response. The amount of overshoot in shear or normal stresses stay constant compared to the steady state value. $\mathcal{N}_2$ however exhibits a negative stress overshoot with a crossover from transient to steady state. Surprisingly we find, $\mathcal{N}_1 \sim -\mathcal{N}_2$ and $\mathcal{N}_3 = \mathcal{N}_1 + \mathcal{N}_2 \sim 0$. After reversing the flow direction from steady flowing state, we find unchanged response of the normal stresses to shear. Nonzero values of $\mathcal{N}_2$ indicates that in forward shear, the stress overshoot phenomena is not limited only to the shear direction, but also has a signature in two perpendicular directions to it. Unchanged magnitude and sign of normal stresses at shear reversal from steady state are indicative of uniform normal forces, devoid of the flowing direction. The distinction of history dependent response in flow reversal is not primarily due to the swapped flow direction, but due to whether the microscopic structure is still close to its equilibrium configuration (and hence only deformed reversibly), or whether it is sufficiently close to the flowing configuration.

4. Local stress fluctuation and pressure

Further support for the hypothesis claimed in the above section comes from a study of the local stress fluctuations, initially suggested by Zausch et al [16]. Defining a local stress element as $\sigma_{xy}^i = -(1/V) \sum_{j \neq i} r_{ij,x} F_{ij,y}$
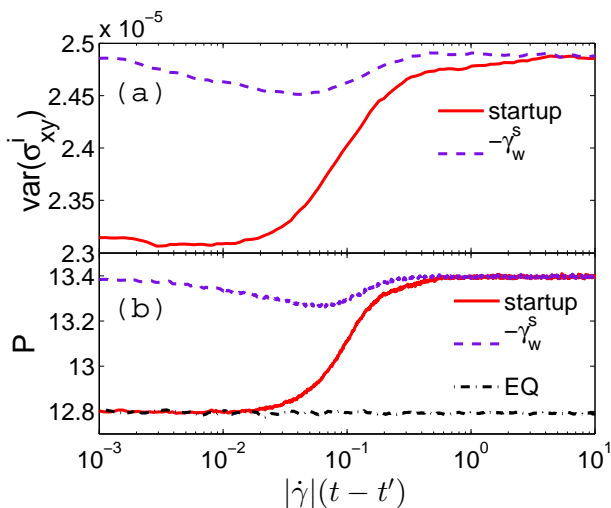
FIG. 4. (Color online) Panel (a): Variance of the local stress distribution corresponding to the stress-strain curves shown in fig.(2). Panel (b): Osmotic pressure for the shear startup and shear reversal from the steady state. Pressure at quiescent state is also marked for comparison. A total of 1000 independent configurations are averaged to obtain the graphics.

such that $\langle\sigma\rangle = \sigma_{\mathrm{pot}}$ is the potential part of the macroscopic stress, the distribution of these local stresses around their average value is computed. The upper panel (a) in fig.(4) depicts the variance of σ_{xy}^i as a function of strain $|\gamma|$ in forward shear from quiescent state and instantaneous reversal from steady flowing state. As already noted in ref. [16], the initial equilibrium configuration is characterized by a variance that is significantly lower than that in the flowing steady state. A steep increase in stress variance around $\gamma \approx 0.1$ is found that coincides with the stress overshoot, separating the reversible elastic regime from the irreversible plastic counterpart. Reversing the shear flow from the steady state regime (denoted with $-\gamma_w^s$), $\mathrm{var}(\sigma_{xy}^i)$ essentially remains at the previously reached level, after exhibiting a small dip below $\gamma \leq 0.1$. In fig.4(b), the osmotic pressure is displayed for the flow startup and reversal from steady state. For the startup case, the increase in the osmotic pressure from one state to another is found without any overshoot at strain ≈ 0.1. In case of shear reversal, the value remains constant at the previously attained value with a small dip. A plausible explanation for the dip can be sought by an argument that instantaneous shear reversal interrupts the established planar Couette flow, thus eventually lowering the fluctuations. The stress variance as well as pressure reaches the forward steady state value as soon as the linear flow profile is re-established in the opposite direction. Identical response of pressure and the fluctuation in particulate stress with strain indicate of an interconnection between these seemingly different quantities.

B. Microstructure

1. Anisotropies in the transient structure

To understand the shear induced anisotropy in the local fluid structure, we measure the angle dependent radial distribution function $g(r,\theta)$ on shear-gradient (x-y) plain. Fig.(5) shows the extra contribution of shear to the microstructure from the homogeneous and isotropic quiescent state, denoted with g_{EQ}. A faint, brown arrow printed on panel (d) and (h) shows the extensional axis while a bold, magenta arrow perpendicular to it in the same panel depicts the compressional axis. Successive points corresponding to the accumulated strain mentioned in fig.(5), is printed in the stress-strain curve (fig.2) for a direct comparison. It is worth mentioning that planar Couette flow is established for all of the reported accumulated strains. As depicted in panel (a-d), in forward shear, the homogeneous state is steadily deformed with development of anisotropies along the extension-compression axis. This feature of the shear induced structural deformation that pushes more particles around the compressional axis while pulling the particles apart along the extensional axis is also reported in molecular simulations [15, 24]. As could be anticipated from the stress-strain relationship, the amount of compression-extension is the maximum at the point of stress overshoot (shown in panel (c)). Panel (e-h) depict the time evolution of the structure at reversed flowing state. Instantaneous shear reversal from steady state results to an exchange between extension-compression axis with an intermediate uniformly compressed state, seen in panel (e). This clearly indicate of an absence of force chains or jamming of colloidal particles [25] in the considered shear rate. The vanishing of the stress overshoot attributes to ceasing of maximal anisotropy along the compression-extension axis present in forward shear. Finally, panel(d) and panel (h) confirms the equivalence of steady state structure in opposite flowing directions without any memory of the flow history.

2. Steady state structure

To conclude the discussion on microstructure, we calculate the steady state structure observed in the local projected quantities $Re[g_{22}^{\alpha\alpha}(r)]$ and $Im[g_{22}^{\alpha\alpha}(r)]$ defined in Eq.(5-6). Recall that the first normal stress can be obtained from $Re[g_{22}^{\alpha\alpha}(r)]$ as $\mathcal{N}_1 = \rho^2\sqrt{2\pi/15}\sum_{\alpha\beta} N_\alpha N_\beta/N^2 \int_0^\infty dr r^3 [\partial V_{\alpha\beta}(r)/\partial r] \times Re[g_{22}^{\alpha\beta}(r)]$. The upper panel of fig.(6) compares the steady state structure $Re[g_{22}^{\alpha\alpha}(r)]$ for the shear startup from a quiescent state as well as the shear reversal from the steady state for $\alpha \in A$-species. We find excellent agreement between the structure in steady state for both directions, indicative of a homogeneously flowing state with equal planar anisotropy devoid of any memory of
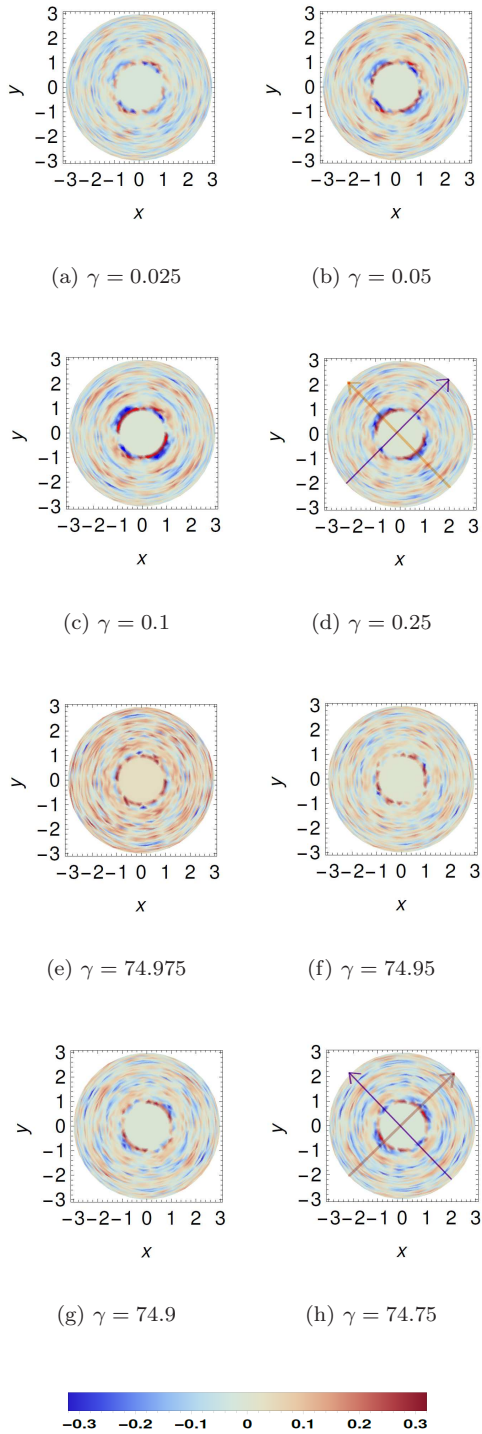
(a) $\gamma = 0.025$　　　　(b) $\gamma = 0.05$

(c) $\gamma = 0.1$　　　　(d) $\gamma = 0.25$

(e) $\gamma = 74.975$　　　　(f) $\gamma = 74.95$

(g) $\gamma = 74.9$　　　　(h) $\gamma = 74.75$

FIG. 5. (Color online) Density plot of $g_{shear}(r,\theta) - g_{EQ}$ in the shear-gradient plain depicted in false colour. States after shear startup from a quiescent state with accumulated strains are indicated in panel (a-d) while panel (e-h) show different states after shear reversal from plastic state with accumulated strain $\gamma = 75$. In panel (d) and (h), extension axis is displayed with faint, brown arrow while compression axis is displayed with bold, magenta arrow. A total of 100 independent simulation runs are averaged and within each run 10 configurations centered around the respective strain value are averaged to obtain the graphics.
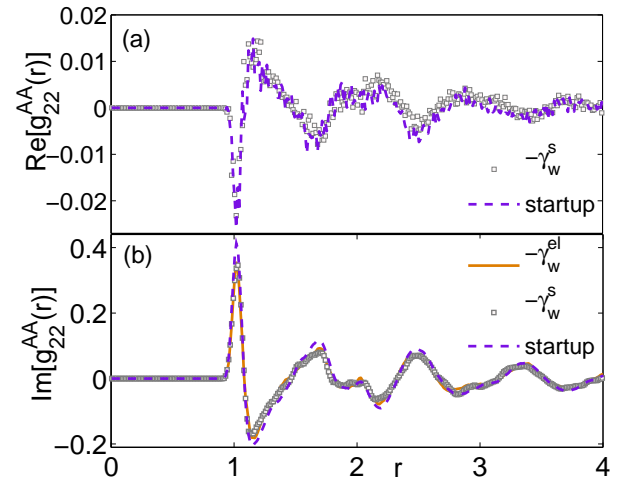

FIG. 6. (Color online) Panel(a) shows steady state $Re[g_{22}^{\alpha\alpha}(r)]$ correlations between $\alpha \in A$-particles, obtained by correlating 250 steady state configurations within a strain window $[50, 75]$ in a single run and then averaging over 20 independent samples for shear start up (magenta, dashed line) and reversal from plastic steady state (square symbol). Panel(b) shows the imaginary part of $g_{22}^{\alpha\alpha}(r)$ correlations between $\alpha \in A$-particles after shear reversal from elastic (brown, solid line) and plastic branch (square symbol) at steady state shear stress $\sigma_{xy} = -0.36$. Sign reversed forward steady state curve (magenta, dashed line) is also shown for comparison.

the quiescent or pre-sheared configuration. The most important contribution to first normal stress is attributed to the nearest neighbour distance structure of the pair correlator. As seen for nearest neighbour distances, particles are squeezed along the compressional axis in the plain and extended along the extensional axis. This results to a positive $\mathcal{N}_1$ at the considered strain rate.

The shear stress on the other hand can be derived from $Im[g_{22}^{\alpha\alpha}(r)]$ as $\sigma_{xy} = -\rho^2 \sqrt{2\pi/15} \sum_{\alpha\beta} N_\alpha N_\beta / N^2 \int_0^\infty dr r^3 [\partial V_{\alpha\beta}(r)/\partial r] \times Im[g_{22}^{\alpha\beta}(r)]$. Panel (b) compares the positional dependence of $Im[g_{22}^{\alpha\alpha}(r)]$ for $\alpha \in A$-species at steady state for two different shear reversal state, denoted by $-\gamma_w^{el}$ and $-\gamma_w^{s}$, to the forward directed steady state. The correlator (sign reversed) in forward shear agrees well with the correlator obtained from the steady reversed flowing states. This result coincides with an earlier claim that at equal moduli of shear stress, the projected structure retains it's shape devoid of the flow history [16]. We found this to hold for reverse flowing states as well and thus extending the claim for first normal stress-structure relation at steady state and numerically validate Eq.(7).

V.   CONCLUSIONS AND OUTLOOK

By employing a dissipative particle dynamics scheme in conjunction to Lees-Edwards boundary condition to soft repulsive colloids, in this article we have discussed the nonlinear rheology of dense colloidal melt under shear flow, specifically the transient and steady state properties after a sudden application of steady strain rate $\dot{\gamma}$, starting from either a quiescent state or various configurations that have been pre-sheared in the opposite direction. Functional dependence of shear and normal stresses as well as osmotic pressure with Péclet number is sought. A crossover from Newtonian to sub-Newtonian regime is found in shear-stress for $Pe > 0.1$ while the normal stresses remain in the sub-Newtonian regime. The osmotic pressure saturates for lower Pe. The binary melt exhibit shear thinning and for much higher strain rates can result into a shear thickening behaviour with a negative $\mathcal{N}_1$ [26].

Stress-strain curves of the pre-sheared configurations are measured along with shear start-up. In addition to the overshoot in shear stress, overshoot in first and second normal stresses is observed at 10% strain amplitude with a step jump in the osmotic pressure as well as in the particulate stress variances. However, once attained the steady state, no stress overshoot is found while unchanged state of pressure and local stress variance emerge in response to shear reversal. This validates the conjecture of shear induced nearest-neighbour cage breaking at startup flow, having a steady state with weak cages that ceases to play any dramatic role when the direction of flow is reversed. An interesting connection can be sought between the fluctuations of the particulate shear and normal stresses with the osmotic pressure, which is beyond the work presented here.

Angle dependent pair correlation function depicts that a uniform exchange of compression-extension axis occurs with a continuous evolution of structure, obtaining a steady Couette flow in relatively short span of time without cluttering or formation of force chains which are a typical signature in athermal systems. We also do not find any shear induced crystallization at the considered shear rates. Maximal anisotropy is exhibited at a strain where stress overshoot appears in forward shear while such maxima cease to exist in the shear reversed states. The steady state structure in both direction containing equal anisotropy confirms an absence of flow history in steady state. The agreement in shear induced structure at steady flowing state validates the relationship between various components of the pair correlator and macroscopic stresses. The change of sign in shear direction attributes to an exchange of extension-compression axis as noted in the imaginary component of the pair distribution function while unchanged structure of the real component of the pair correlator confirms of a positive $\mathcal{N}_1$ for both directions of shear. In a similar spirit to Eq.(7-8), relation between $\mathcal{N}_2$ and $\mathcal{P}$ to the components of pair correlator can be obtained [21] and an unchanged structure at equal stresses can be found. However, such studies should be performed at larger strain rates with the melt been quenched deep into the glassy state, which is outside the scope of the presented work. We seek for experimental measurement in dense supercooled melt to verify the claims presented in this article.

[1] K. Binder and W. Kob, *Glassy materials and disordered solids : an introduction to their statistical mechanics* (World Scientific Pub. Co., Singapore, 2005).

[2] R. G. Larson, *The structure and rheology of complex fluids* (Oxford University Press, New York, 1999).

[3] F. Boyer, O. Pouliquen, and E. Guazzelli, Journal of Fluid Mechanics **686**, 5 (2011).

[4] T. F. F. Farage, J. Reinhardt, and J. M. Brader, Phys. Rev. E **88**, 042303 (2013).

[5] T. N. Phung, J. F. Brady, and G. Bossis, J. Fluid. Mech. **313**, 181 (1996).

[6] J. Seth, L. Mohan, C. Champagne, M. Cloitre, and R. Bonnecaze, Nature Materials **10**, 838 (2012).

[7] S. R. Rastogi, N. J. Wagner, and S. R. Lustig, J. Chem. Phys. **104**, 9234 (1996).

[8] N. Koumakis, P. Ballesta, R. Besseling, W. C. K. Poon, J. F. Brady, and G. Petekidis, AIP Conference Proceedings **1518**, 365 (2013).

[9] J. D. Moore, S. T. Cui, H. D. Cochran, and P. T. Cummings, Phys. Rev. E **60**, 6956 (1999).

[10] Y.-G. Tao, W. K. den Otter, and W. J. Briels, Macromolecules **39**, 5939 (2006).

[11] J. Zausch, J. Horbach, M. Laurati, S. U. Egelhaaf, J. M. Brader, T. Voigtmann, and M. Fuchs, J. Phys.: Condens. Matter **20**, 404210 (2008).

[12] F. Frahsa, A. K. Bhattacharjee, J. Horbach, M. Fuchs, and T. Voigtmann, J. Chem. Phys. **138**, 12A513 (2013).

[13] N. Koumakis, A. B. Schofield, and G. Petekidis, Soft Matter **4**, 2008 (2008).

[14] J. G. Kirkwood, The Journal of Chemical Physics **14**, 180 (1946).

[15] H. J. M. Hanley, J. C. Rainwater, and S. Hess, Phys. Rev. A **36**, 1795 (1987).

[16] J. Zausch and J. Horbach, Europhys. Lett. **88**, 60001 (2009).

[17] S. Karmakar, E. Lerner, and I. Procaccia, Phys. Rev. E

82, 026104 (2010).

[18] J. M. Brader, M. Siebenbürger, M. Ballauff, K. Reinheimer, M. Wilhelm, S. J. Frey, F. Weysser, and M. Fuchs, Phys. Rev. E **82**, 061401 (2010).

[19] J. D. Weeks, D. Chandler, and H. C. Andersen, J. Chem. Phys. **54**, 5237 (1971).

[20] M. Abramowitz and I. A. Stegun, *Handbook of Mathematical Functions: With Formulas, Graphs, and Mathematical Tables* (Dover, New York, 1964).

[21] H. H. Gan and B. C. Eu, Phys. Rev. A **45**, 3670 (1992).

[22] S. Mandal, M. Gross, D. Raabe, and F. Varnik, Phys. Rev. Lett. **108**, 098301 (2012).

[23] S. Papenkort and T. Voigtmann, The Journal of Chemical Physics **140**, 164507 (2014).

[24] N. Koumakis, M. Laurati, S. U. Egelhaaf, J. F. Brady, and G. Petekidis, Phys. Rev. Lett. **108**, 098303 (2012).

[25] M. E. Cates, J. P. Wittmer, J.-P. Bouchaud, and P. Claudin, Phys. Rev. Lett. **81**, 1841 (1998).

[26] J. Mewis and N. J. Wagner, *Colloidal Suspension Rheology* (Cambridge University Press, 2012).